Check for updates

Optimizing Hole Shape and Improving Surface Quality of Inconel 718 Alloy by High-Temperature Chemical Assisted Laser Processing

Xi Wang[1] · Bing Han[2] · Martin Ehrhardt[3] · Dongsik Kim[4] · Fengyun Zhang[1] · Jin Wang[1] · Pingping Wang[1] · Shufeng Sun[1]

Abstract

High-quality micro-hole processing of superalloy has always been challenging work in the aerospace and automobile industries. A novel high-temperature chemical assisted laser processing technology was investigated to provide an one-step in-situ method for eliminating defect layer and optimizing hole shape, thereby solving the two challenges of surface roughness and taper in micro-hole processing. An environmental-friendly chemical liquid was adopted. Chemical etching occurred at the interface of the material-modified layer in the local high-temperature environment to minimize surface roughness, and the chemical liquid played a role of a confinement layer, limiting the expansion of the high-temperature gas and plasma leading to the laser plasma ablation pressure applied to the substrate material. The influences of defocus and laser pulse interval on hole formation and geometry characteristics, taper angle, and surface roughness were investigated. The experiment results revealed that when the laser pulse interval was less than or equal to 0.1 ms, the blind hole shape was close to being cylindrical, when the laser pulse interval was 1 ms, the blind hole was a conical shape with a deeper depth. The interaction mechanism in high-temperature chemical assisted laser drilling was analyzed, including laser plasma ablation pressure, and liquid jet following cavitation bubble collapse in the liquid confined region. This study has a potential application in the field of super-alloy drilling.

Keywords High-temperature chemical · Laser processing · Inconel 718 · Plasma · Hole shape optimization

1 Introduction

Inconel 718 alloy is widely applied in the aerospace and automobile industries for the hot sections of gas turbine engines such as turbine disks, blades, and casings because of its high strength, heat resistance, and corrosion resistance character. Nickel-based superalloys currently constitute more than half of the weight of advanced aircraft engines. High-quality micro-hole processing has always been challenging work for cooling holes on turbine blades and injection nozzles in vehicle engines [1]. Poor quality of the micro-holes may initiate cracks inside the device structure and reduces their reliability. For example, microcracks originating from the wall of the cooling holes account for 80 percent of blade fractures, in which, the fatigue cracks are more than half of them [2]. The quality of micro-holes needs to be optimized to improve the stability and service life of the device. Therefore, it is critical to provide a controllable hole surface quality and shape machining technology of Inconel 718 for engineering applications.

✉ Bing Han
hanbing@njust.edu.cn

✉ Shufeng Sun
sunshufeng@qut.edu.cn

1 Collaborative Innovation Center for Green Intelligent Laser Manufacturing Technology and Equipment of Shandong Province, School of Mechanical and Automotive Engineering, Qingdao University of Technology, Qingdao 266520, China

2 School of Electronic and Optical Engineering, Nanjing University of Science & Technology, Nanjing 210094, China

3 Leibniz Institute of Surface Engineering (IOM), 04318 Leipzig, Germany

4 Department of Mechanical Engineering, Pohang University of Science and Technology (POSTECH), Pohang 37673, Republic of Korea

The conventional micro-hole machining techniques include mechanical drilling [3], electrical discharge machining (EDM) [4], electrochemical machining (ECM) [5], laser drilling [6], etc. The advantages of mechanical drilling are a high depth/diameter ratio and a wide range of processing materials. However, the drill bit is easily broken, and the processing surface quality is poor. EDM can only process conductive materials, and the heat effect of electric spark causes thermal defects (microcracks, recast layers, and heat-affected zones) on the hole wall. For ECM, there is no thermal effect defect on the surface of the material. However, ECM is limited to processing metal materials and has a low processing efficiency. Laser drilling is a novel micro-drilling method with benefits including fast machining speed, high efficiency, high accuracy, and no tool loss. However, when laser drilling is carried out in the air, some defects, including heat-affected zones, micro-cracks, and recast layers, are unavoidable, all of which hurt the material properties. Although the picosecond and femtosecond lasers with shorter pulses can reach micro/nanoscale precision in both shapes and dimensions with minimal heat-affected zone, the high cost and low material removal rate limit the potential prospect in specific application areas. For example, the material removal rate of femtosecond laser drilling is only about 0.054 mm^3/min [7].

Various water-assisted laser machining technologies have been proposed to reduce the thermal defects and improve the processing quality [8], such as underwater laser processing [9], laser processing under flowing water layer [10], water jet-assisted underwater laser processing [11, 12], and water jet-guided laser processing [13, 14]. For laser processing under the flowing water layer, low pressure and low flow rate water impact the workpiece surface to generate a thin and flowing water layer. The flow liquid layer thickness is usually less than 1 mm. For water jet-assisted underwater laser processing, a high-pressure coaxial or paraxial water jet is delivered along with the focused laser beam to the workpiece to remove the molten material. It produces very less turbulence and gas bubbles in the water. The high-pressure water jet can remove the material at its soft-solid status below its melting temperature. In the case of water jet-guided laser processing, the laser beam is guided inside the water jet and conveyed to the workpiece surface. The water jet can efficiently expel the molten material and cool the remaining material. Although the thermal defect may be effectively minimized in water-assisted laser processing, it is easy to create burrs on the surface and form a processing taper as the workpiece thickness increases. The defect layer can be removed, and the hole taper can be optimized after a long time of immersion in a chemical liquid such as salt solutions, alkaline liquids, and acid liquids [15–18]. However, it takes much time to completely remove the defective layer, and there is a possibility that the substrate material may also be corroded after a long treatment time. Therefore, it is critical to realize the controllable processing of the micro-hole taper while ensuring high surface quality.

A novel high-temperature chemical assisted laser processing technique was investigated in this study to provide a method of one-step in-situ defect layer removal and optimization of hole shape and surface quality, thereby solving the two critical challenges of surface roughness and taper in micro-hole machining. The environmental-friendly liquid, the mixture of hydrochloric acid and sodium nitrate solution, was adopted as the chemical liquid. Because of its strong corrosion resistance character for Inconel 718, the reaction speed between low concentration chemical liquid and Inconel 718 was extremely slow and negligible at room temperature. In the laser-induced local high-temperature environment, the chemical etching was accelerated at the interface of the material-modified layer. The substrate material in other regions was not affected by the chemical liquid due to its relatively low temperature. Furthermore, the chemical liquid acted as a confinement layer limiting the expansion of the high-temperature gas and plasma on the material-modified layer. The influences of laser defocus, pulse interval, and chemical liquid layer confinement on hole formation and geometry characteristics, taper angle, and surface roughness were investigated systematically. The interaction mechanism of high-temperature chemical assisted laser processing was analyzed. The pressure generated by laser plasma in the liquid confined region was theoretically approximated, and the development of fluid dynamics was numerically calculated.

2 Experimental and Numerical Methods

2.1 Experimental Description

Figure 1A shows the experimental setup of high-temperature chemical assisted laser processing. A 1064 nm nanosecond laser system (IPG YLPN-1-100-200-R) was used in this study. The pulse repetition rate was 20 kHz and the maximum power was 200 W. The laser beam with Gaussian distribution was focused onto the workpiece through the lens. When measured in the air, the spot size of the focused laser beam was about 50 μm. The Inconel 718 sample (20 mm × 20 mm × 1 mm) was mounted in an acrylic container (100 mm × 100 mm × 20 mm) that was placed on a three-axis displacement stage. The pump and nozzle were used to inject the chemical liquid into the container. The laser beam was irradiated into liquid from air. When the sample was positioned at the focus in the air, the defocus was defined as $d = 0$ mm, as displayed in Fig. 1b. The sample surface moving up and down was represented by the positive and negative values of defocus. The z-axis lifting platform was moved to change the defocus. The distance
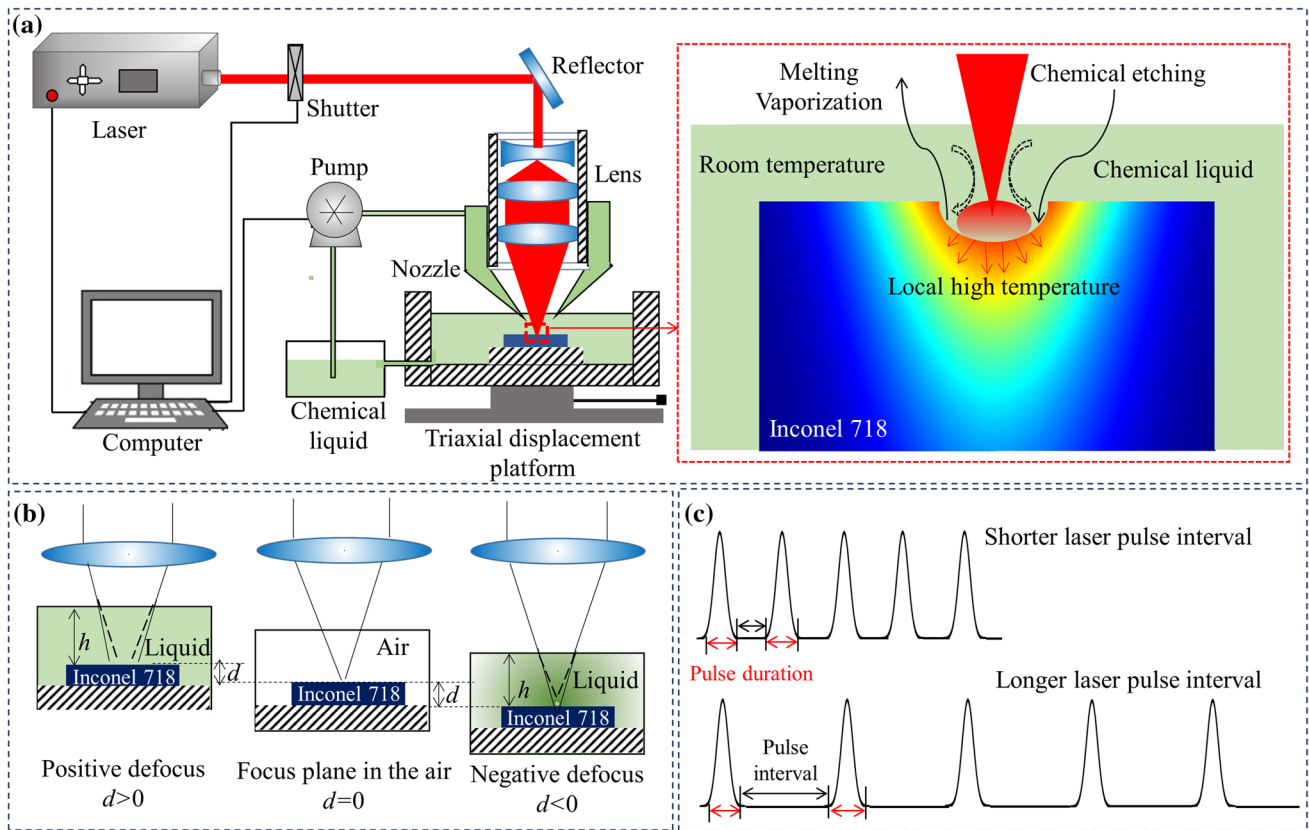
Fig. 1 Experimental detail of high-temperature chemical assisted laser processing. **a** The schematic diagram of the experimental setup. **b** Positive and negative defocus. **c** The timing chart of laser in time domain distribution for different pulse intervals

between the sample upper surface and the liquid layer surface was indicated by the liquid layer thickness h. In Fig. 1c, the laser duration was 100 ns, the adjacent pulse interval was varied by an electronic shutter. When the laser power density is more than 10^8 W/cm^2 during nanosecond pulse laser interaction with matter, the material breakdown is induced resulting in plasma at the laser focal point. The breakdown threshold of solid material is usually lower than that of a liquid. The laser power density was 6×10^9 W/cm^2 in the experiment, which was greater than the breakdown threshold of Inconel 718 ($10^8 \sim 10^9$ W/cm^2), but lower than the breakdown threshold of liquid ($10^{10} \sim 10^{11}$ W/cm^2) [19,

20]. Moreover, the chemical liquid layer played a restrictive role and constrained the high-temperature vapor and plasma expansion outward.

The common composition of Inconel 718 is listed in Table 1, which comprises nickel, chromium, niobium, molybdenum, iron, and other micro-elements such as carbon and silicon, etc. The used IN718 sample in this study is a casting state cold-rolled plate of 2 mm thickness provided by Shanghai Longjin Special Steel Group Co., Ltd. It was processed into 20 mm×20 mm×2 mm plates by wire cut electrical discharge machine. The surface was polished and cleaned with alcohol to remove surface impurities and stains.

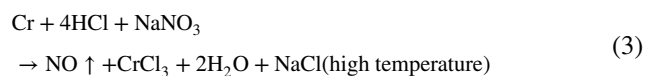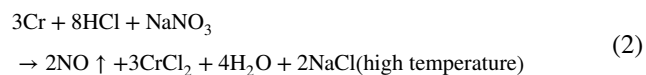**Table 1** The material compositions (wt%) of the used Inconel 718

Element	Ni	Cr	Nb	Mo	C	Mn
wt%	50.00–55.00	17.00–21.00	4.75–5.5	2.80–3.30	<0.08	<0.35
Actual	53.66	18.41	4.92	2.87	0.03	0.08
Element	Si	Cu	Co	Al	Ti	Fe
wt%	<0.35	<0.30	<1.00	0.20–0.80	0.65–1.15	Balance
Actual	0.09	0.13	0.34	0.5	0.96	17.9

The elemental composition was measured by energy dispersive X-ray spectroscopy (EDS) SEM and listed in Table 1.

A mixture solution of hydrochloric acid and sodium nitrate (1 mol/L NaNO$_3$ and 1 mol/L HCl) is adopted as the chemical liquid in the experiment [21]. Inconel 718 has the character of corrosion resistance, therefore, the reaction speed between Inconel 718 and low concentration chemical liquid is extremely slow at room temperature and can be negligible. The high-temperature environment promotes the occurrence of chemical etching. The substrate material does not participate in the reaction due to its strong chemical resistance at a relatively lower temperature. The chemical etching only happens around the modified layer of the laser-irradiated region which can reduce the surface roughness. When the laser is turned on, the hole entrance is in a local high-temperature region, the molten Inconel 718 reacts with the chemical liquid and is no longer deposited on the sample surface. When the laser is turned off, the local high-temperature environment around the hole entrance vanishes, and the chemical reaction stops. Hence laser acts as a regulator of the temperature field controlling the chemical reaction during high-temperature chemical assisted laser processing. Most of the byproducts of chemical reactions are gas and water-soluble compounds. The removal reactions of the main alloy elements during the high-temperature chemical assisted laser processing are analyzed here, including Ni, Cr, Nb, and Fe. For nickel, the following is the chemical reaction process:

$$Ni + 2HCl + 2NaNO_3$$
$$\rightarrow 2NaCl + Ni(NO_3)_2 + H_2 \uparrow \text{(high temperature)} \quad (1)$$
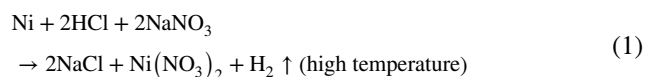
For chromium, it can slowly dissolve in dilute hydrochloric acid and dilute sulfuric acid at room temperature. However, chromium does not dissolve in highly concentrated acids such as concentrated nitric acid, because the surface produces an oxide film and shows a passivated state. In the local high-temperature environment, chromium can react with the low concentration mixture solution of hydrochloric acid and sodium nitrate.

$$3Cr + 8HCl + NaNO_3$$
$$\rightarrow 2NO \uparrow + 3CrCl_2 + 4H_2O + 2NaCl \text{(high temperature)} \quad (2)$$

$$Cr + 4HCl + NaNO_3$$
$$\rightarrow NO \uparrow + CrCl_3 + 2H_2O + NaCl \text{(high temperature)} \quad (3)$$

Niobium metal is extremely stable and does not react with an acid solution at room temperature, the following reaction may occur in high-temperature environments:

$$6Nb + 10HCl + 10NaNO_3$$
$$\rightarrow 3Nb_2O_5 + 10NO \uparrow + 5H_2O + 10NaCl \text{(high temperature)} \quad (4)$$
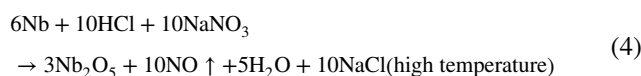
NbC has good chemical stability and is only soluble in a mixture of HNO$_3$ and HF. It does not react with low concentration HCl and NaNO$_3$ mixed solution. Iron can react with low concentration acid solutions at room temperature, and react with halogens when heated. The removal reaction of iron during the high-temperature chemical assisted laser processing is listed below:

$$Fe + 4HCl + NaNO_3$$
$$\rightarrow 2H_2O + NaCl + NO \uparrow + FeCl_3 \text{(high temperature)} \quad (5)$$
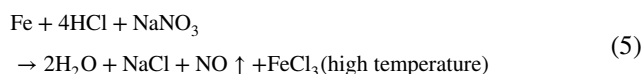
After high-temperature chemical assisted laser processing of Inconel 718, the samples were cleaned in deionized water and dried for measurement. The micro-morphology of the sample was measured directly without solution heat treatment and aging heat treatment. The microhole was polished along the longitudinal direction to expose the microhole's longitudinal section. Scanning electron microscopy (SEM Merlin Compact, Zeiss) was used to evaluate the surface morphology, and energy dispersive X-ray spectroscopy (EDS) was used to measure the elemental content. The cross-section profile and hole shape were measured using a laser confocal microscope (LCM, VK-X1000, Keyence).

2.2 Numerical method

Numerical simulation is important in analyzing the behavior of fluid dynamics in high-temperature chemical assisted laser processing. When a laser pulse interacts with a rigid target in the liquid, the solid material is gasified and ionized, resulting in a high-pressure plasma. The plasma expands outward, creating an isotropic shock wave that transmits its energy to the surrounding liquid, resulting in a thin layer of vapor around the plasma. This is the initial stage of the cavitation bubble. The cavitation bubble expands until it reaches its maximum radius and the pressure inside the bubble balances the pressure of the liquid. The bubble begins to collapse when the pressure inside the gas decreases to sub-atmospheric levels, resulting in the formation of a liquid jet. It is necessary to model the evolution of the fluid dynamics to analyze the effect of the cavitation bubble and liquid jet on material removal.

As presented in Fig. 2, a two-dimensional axisymmetric model is developed to analyze fluid dynamics. A micro-hole with a size of 200 µm × 100 µm is pre-set on the substrate surface while modeling the flow field evolution under the multi-pulse laser. The laser beam is directed vertically down to the sample's upper surface. Axis r is the direction of beam radius, and z is the symmetry axis. It is computed numerically using the Finite Volume Method and Open Field
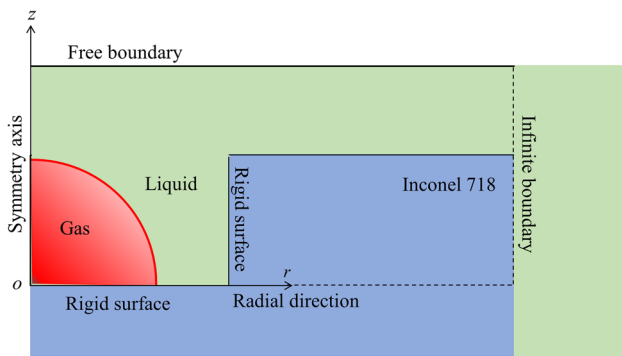
Fig. 2 Schematic diagram of flow field evolution calculation model

Operation And Manipulation (OpenFOAM). OpenFOAM is an open-source CFD software programmed in C + + based on the finite volume method [22]. The volume of fluid (VOF) method is used to track the liquid-gas interface in the flow. The liquid phase and gas phase is treated as a single phase, with a volume proportion of one of the phases ranging from 0 to 1. Two phases share a single set of momentum equations. The volume fraction of the two phases depicts the density of the flow field, as indicated in Eq. (6) [23]:

$$\rho_f = \varepsilon \rho_l + (1 - \varepsilon)\rho_g \tag{6}$$

where, ρ_f, ρ_l and ρ_g represent the density of the flow field, liquid phase, and gas phase, respectively. ε is the water volume fraction. When $\varepsilon = 1$, the cell contains solely liquid. When $\varepsilon = 0$, the cell contains solely gas. Therefore, the interface is a series of cells of $0 < \varepsilon < 1$ rather than a sharp surface. The mass conservation equation of one phase is solved to provide the interphase displacement [23], as indicated in Eq. (7):

$$\frac{\partial(\varepsilon\rho_l)}{\partial t} + \nabla \cdot \left(\varepsilon\rho_l \vec{U}\right) = 0 \tag{7}$$

where $\vec{U}$ represents the velocity vector in the flow. The Navier–Stokes equations are numerically solved using the standard solver compressible Interfoam.

The state equation for the constant amount of vapor inside the bubble is the ideal gas equation. Surface tension, compressibility, and viscosity for both gas and liquid are included, whereas condensation, evaporation, and heat conduction are neglected. The initial pressure of the gas is estimated to be 1×10^7 Pa. The infinite boundary condition is defined as the pressure on the boundary equaling the atmospheric pressure, i.e., 1×10^5 Pa, and the gradient of the velocity is 0. Because the chemical liquid in this study has a low concentration, the surface tension and kinetic viscosity are assumed to be similar to water. The surface tension of gas and chemical liquid is 0.07 N/m. The kinetic viscosity of gas and chemical liquid is 1.589×10^{-5} and

10^{-6} m²/s, respectively. The density of gas and chemical liquid is 1 and 1060 kg/m³. The initial temperature is room temperature (293 K). Because the bubble interaction geometry is axisymmetric, hexahedral wedges are utilized for meshing.

3 Experimental Results

3.1 The Change of Focal Point Position of the Laser Beam in the Chemical Liquid

First, it is necessary to research the focal point and transmission character of the laser beam in the chemical liquid. In Fig. 3**a**, when a laser beam is transmitted from the air to the liquid, the laser focal point shifts downward due to that the refractive index of the chemical liquid is higher than that of air, resulting in a focal length extension. The laser intensity exceeds the breakdown threshold of Inconel 718 and is less than that of chemical liquid, therefore, the workpiece is ionized and the vapor-plasma plume is formed on the sample surface. Consequently, the focus position in the liquid is the joint effect of the light refraction and the vapor-plasma plume.

It assumes that the refractive index of chemical liquid is approximately equal to that of water. If the light refraction between the air and liquid surface is only considered, the change distance of the laser focus in the chemical liquid can be calculated by Eq. (8) according to Snell law [24]:

$$d = \frac{h\sqrt{n_{liquid}^2 f^2 + n_{liquid}^2 \omega_0^2 - \omega_0^2}}{f} - h \tag{8}$$

where h, n_{liquid}, f and ω_0 represent the liquid layer thickness, the liquid refractive index, the lens focal length, and laser beam radius before the focusing lens, respectively. It can be seen that the change distance of the focal point is proportional to the liquid layer thickness h. In Eq. (8), the refractive index of the chemical liquid is approximately equal to water ($n_{liquid} \approx 1.33$), $f = 50$ mm, $\omega_0 \approx 1$ mm. When the light refraction is only considered, the theoretical relationship between the focus change distance and liquid layer thickness is shown as the red dashed line in Fig. 3 (b), in which the negative sign means that the focus moves downward compared with the original focus position in the air. In addition, the influence of the vapor-plasma plume on the focus change cannot be ignored. Equation (9) is used to describe the plasma free-electron evolution [25]:

$$\frac{d\rho}{dt} = \left(\frac{d\rho}{dt}\right)_{mp} + \eta_{casc}\rho - \eta_{rec}\rho^2 \tag{9}$$
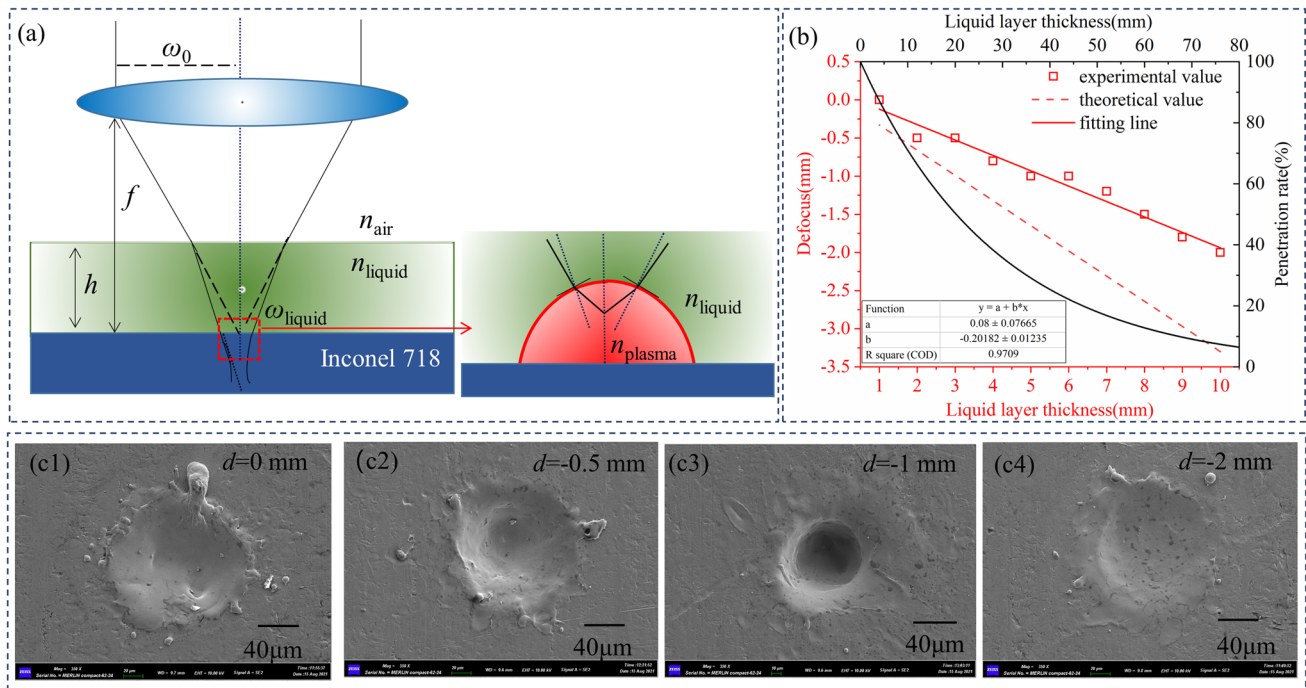
Fig. 3 Effects of the defocus on the blind hole morphology. **a** Diagram of laser refraction in the air–liquid interface. **b** The focus change distance and the laser penetration rate at the different liquid layer thicknesses. **c** SEM images of Inconel 718 at different defocus by high-temperature chemical assisted laser processing, $h=5$ mm, $N=1$, laser pulse interval is 0.1 ms

where $(d\rho/dt)_{mp}$ represents multi-photon ionization, $\eta_{casc}\rho$ represents cascade ionization, and $\eta_{rec}\rho^2$ represents recombination, respectively. According to Eq. (9), the shape and intensity of plasma are directly connected to free electrons. The radial and axial distribution of free electron density decrease with distance from the center due to expansion. The refractive index, which governs the transmit characteristic of the laser beam, is determined by the electron density distribution of the plasma. The refractive index of plasma can be calculated by Eq. (10) [26]:

$$n_{plasma} = n_{en} - \frac{\rho}{\rho_{cr}} \tag{10}$$

where, n_{plasma} and n_{en} represent the refractive index of plasma and environmental medium, ρ and ρ_{cr} represent the electron density and critical electron density of plasma, respectively. When a thin layer of high-temperature vapor and plasma plume containing ions, free electrons, and neutral particles is generated on the sample surface, the refractive index is less than that of the surrounding liquid environment ($n_{plasma} < n_{liquid}$) leading to a shortening of focal length.

The red square symbols in Fig. 3b shows the experimental value of defocus when the blind hole depth is maximum under various liquid layer thickness. It is found that the focus change distance under liquid is less than the theoretical value only considering light refraction. It validates that the laser

focus in the liquid is a combination of laser beam refraction increasing focal length and plasma shortening the focal length. The absorption coefficient of the chemical liquid is approximately equal to that of the water at 1064 nm laser (34.2438 m^{-1}) [27], the black curve in Fig. 3b shows the laser penetration rate in the different liquid layer thicknesses according to Beer-Lambert law. The liquid layer thickness in this study is 5 mm, the laser penetration rate is about 92%. In Fig. 3c, $h=5$ mm, the SEM images of Inconel 718 at different defocus are displayed. It can be seen that when the defocus is -1 mm, the hole is the deepest. Therefore, the defocus of − 1 mm is at or near the actual focus for the liquid layer thickness of 5 mm.

3.2 The Optimization of Shape Hole in High-temperature Chemical Assisted Laser Processing

An interesting result was found in the experiment, that was, the interval between two adjacent pulses had a great impact on the hole shape. High-repetition rate laser was easy to produce the local heat accumulation effect leading to boiling bubbles in the chemical liquid which significantly weaken the laser absorption and produced a rough ablation surface. Therefore, a low pulse repetition rate laser of less than 20 kHz was adopted to weaken the undesired heat effect. The electronic shutter controlled the number of pulses passed,

thereby adjusting the pulse interval. The pulse interval was adjusted to 0.01 ms, 0.1 ms, 1 ms, and 10 ms. The experimental results found when the laser pulse interval was less than or equal to 0.1 ms, the blind hole shape was close to being cylindrical, yet when the laser pulse interval was equal to or more than 1 ms the blind hole changed to a conical shape. The SEM image of surface morphology and three-dimensional morphology of pulse intervals of 0.1 ms and 1 ms are shown in Fig. 4a, b. The hole cross-section profile is displayed in Fig. 4c. The hole taper angle is calculated using the following equation:

$$\alpha = \arctan\left(\frac{d_1 - d_2}{2D}\right) \tag{11}$$

where α is the taper angle, $d1$ is the entrance diameter, $d2$ is the exit diameter, and D is the hole depth.

The blind hole taper angle in Fig. 4a is about 13° when the pulse interval was 0.1 ms. The taper angle in Fig. 4b is about 50° when the pulse interval was 1 ms. The difference in hole taper is because the dominant material removal mechanism is changed at different stages in the process of high-temperature chemical assisted laser processing. When the material is ablated in the liquid environment, melting, vaporization, plasma plume, cavitation bubble, and liquid jet appear successively on the material surface [28]. In Fig. 1c above, the whole process is divided into two stages, the first stage is pulse duration and the second stage is pulse interval. In the first stage, a vapor-plasma plume induced by laser is present at the hole entrance. The expansion of plasma induces a large amount of pressure and promotes the instantaneous ejection of molten and vaporized material from the surface and micro-hole reducing the taper of the micro-hole. In the second stage, the vapor-plasma plume

gradually attenuates and annihilates. The starting time of cavitation bubble nucleation is within one microsecond after pulse duration. The cavitation bubble collapse at about a few hundred microseconds. Following bubble collapse, the liquid jet is induced resulting in the impact on the material [29]. The jet pushes the chemical liquid into the hole removing the softening layer by chemical etching and jet impact force. The etching morphology is affected by the shape of the jet showing an inevitable taper. The influence mechanism detail of the laser pulse interval on the hole shape will be discussed in Sect. 4.

3.3 The improvement of hole surface quality in high-temperature chemical assisted laser processing

Figure 5a1, b1 show the top view and side view of the blind hole of laser processing Inconel 718 in the air. It can be seen that the ejected material re-deposits at the hole entrance. The area where melting and re-solidification occurs is defined as the recast layer. The side view in Fig. 5b1 presents the presence of the recast layer along the inner wall. The area pointed out by the red arrow is the recast layer. In this area, the molten nickel alloy material does not splash out from the hole. After re-solidification, the grain is reconstituted, and the tissue morphology is different from the original material. Figure 5a2, b2 are the top view and side view of the blind hole of high-temperature chemical assisted laser processing. There are no obvious residual debris deposits on the hole entrance and no transition area at the hole sidewall edge. The boundary between the hole sidewall and the matrix material is visible. It indicates that high-temperature chemical assisted laser processing has the advantage to remove the recast layer. Inconel 718 is a precipitation-reinforced
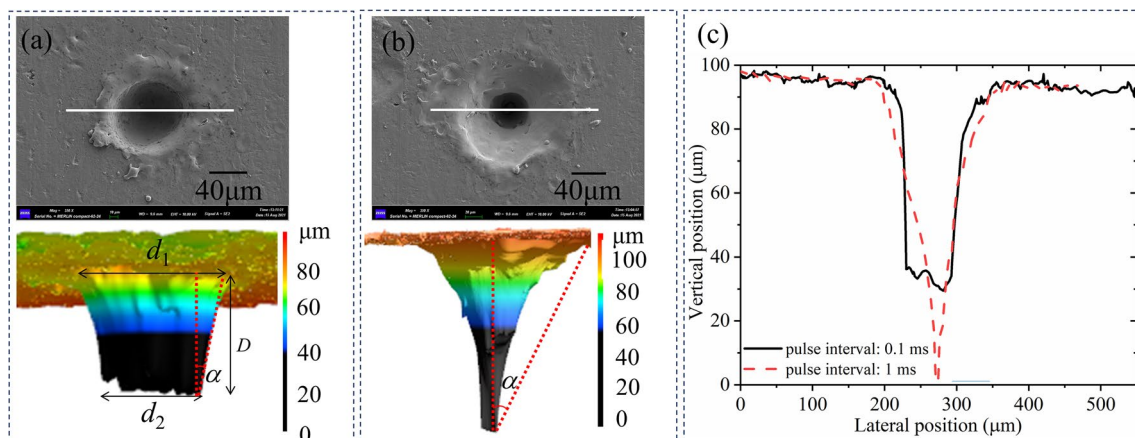

Fig. 4 SEM image of surface morphology, three-dimensional morphology, and cross-section profile for pulse intervals of 0.1 ms and 1 ms. $I_0 = 6 \times 10^9$ W/cm², $h = 5$ mm, $N = 5$, $d = -1$ mm. **a** The pulse interval is 0.1 ms. **b** The pulse interval is 1 ms. **c** The cross-section profiles of the two blind holes
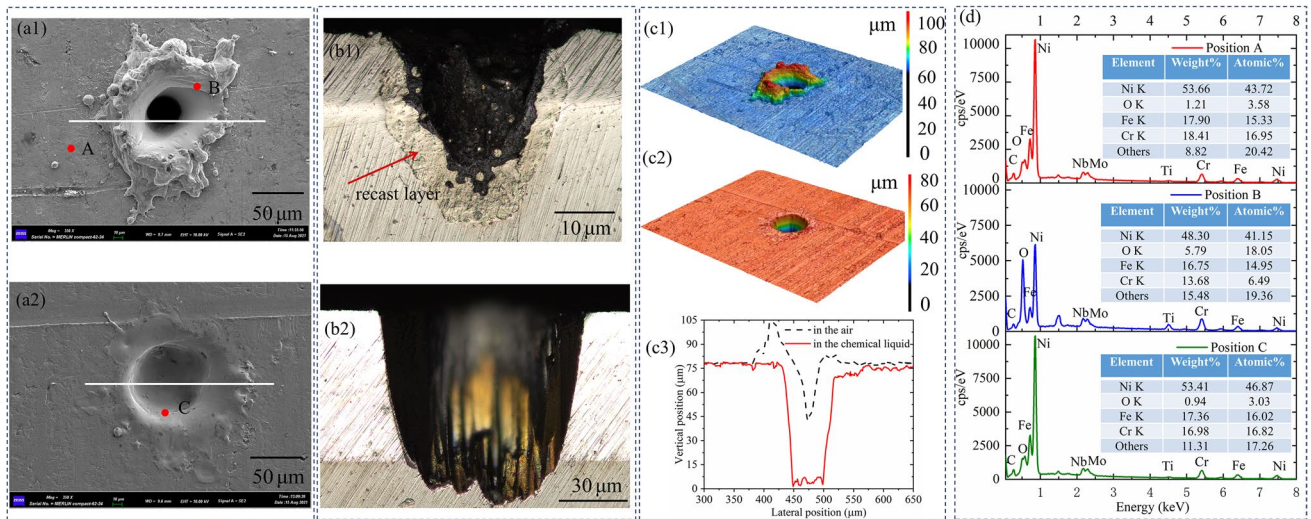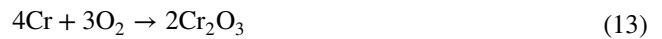
Fig. 5 The comparison of laser processing Inconel 718 in the air and chemical liquid. $I_0 = 6 \times 10^9$ W/cm², $N = 5$, and the laser pulse interval was 0.1 ms. $h = 5$ mm, $d = -1$ mm. **a1**, **b1** The top view and side view of the blind hole of laser processing in the air. **a2**, **b2** The top view and side view of the blind hole of high-temperature chemical assisted laser processing. **c1**, **c2** Surface roughness of laser processing Inconel 718 in the air and high-temperature chemical assisted laser processing Inconel 718. **c3** The cross-section profiles comparison. **d** Energy spectrum diagram of positions A, B, and C

high-temperature alloy and consists of γ matrix phase, γ′ strengthened phase (Ni₃(Al, Ti)), γ″ strengthened phase (Ni₃Nb), delta equilibrium temperature phase (Ni₃Nb), laves harmful phase and a small amount of carbide. The proper heat treatment process promotes the precipitation of γ′ and γ″. In this study, the micro-morphology of the sample was measured directly without solution heat treatment and aging heat treatment. Moreover, the alloy undergoes rapid melting and rapid cooling in the recast layer region, the γ′ phase and γ″ phase may not have enough time to precipitate, so the phase structure of the alloy is not investigated. In Fig. 5c1, the surface roughness of hole entrance S_a is about 8.76 μm. In Fig. 5c2, the surface roughness of the hole entrance S_a is about 0.42 μm. Figure 5c3 reveals the drilling depth of Inconel 718 in high-temperature chemical assisted laser processing is about two times higher than laser direct processing in the air. The result indicates that high-temperature chemical assisted laser processing can effectively improve the hole surface quality by reducing recast layer formation and surface roughness.

Compared to laser processing in the air, the composition of the hole sidewalls changes in high-temperature chemical assisted laser processing. The EDS analysis was utilized to detect the element content before and after laser processing, as shown in Fig. 5d. Point A is the initial sample before laser processing. Points B and C are the hole sidewall after laser processing in the air and chemical liquid, respectively. In comparison to the original sample, the oxygen element content of point B increases after laser processing in the air, indicating the occurrence of an oxidation reaction. The

possible oxides generation is listed in Eq. (12)–(16). For nickel, there are three kinds of oxides existed, that is, NiO, Ni₃O₄, and Ni₂O₃. Ni₂O₃ can remain stable only at low temperatures. When Ni₂O₃ is heated to 400~450℃, it dissociates into Ni₃O₄, which is subsequently converted to NiO as the temperature rises. Hence, nickel (II) oxide is formed after nickel interacts with oxygen. This reaction occurs at a temperature of 500~1000 °C.

$$2Ni + O_2 \rightarrow 2NiO \tag{12}$$

$$4Cr + 3O_2 \rightarrow 2Cr_2O_3 \tag{13}$$

$$3Fe + 2O_2 \rightarrow Fe_3O_4 \tag{14}$$

$$2Mo + 3O_2 \rightarrow 2MoO_3 \tag{15}$$

$$4Nb + 5O_2 \rightarrow 2Nb_2O_5 \tag{16}$$

The oxidation reaction results in the formation of an oxide layer, which weakens the mechanical properties and corrosion resistance of superalloy. Therefore, it is critical to avoid the formation of the oxide layer. The whole workpiece is immersed in liquid and isolated from the air. The oxygen element content in point C decreases significantly after high-temperature chemical assisted laser processing. The melting point of Inconel 718 is around 1400 °C. The molten particles are ejected into the chemical liquid to generate products dissolved in water, preventing them from depositing on the

sample surface again. The heated Inconel 718 which has not yet melted reacts with the chemical liquid in the local high-temperature environment to reduce the surface roughness. Therefore, high-temperature assisted laser processing can effectively prevent oxide layer formation and reduce surface roughness.

4 Discussion

4.1 The Pressure Generated by the Laser Plasma in the Liquid Confined Region at the First Stage

To explore the mechanism of high-temperature chemical assisted laser processing and find the influential factor of hole shape, the pressure generated by the laser plasma in the liquid confined region is estimated. The laser-induced plasma is generated during the first hundreds of nanoseconds after the laser pulse. The liquid constrains the plasma expansion leading to a recoiling pressure on the material. The vaporization and part of melted material can be effectively removed away from the ablation area under the action of the recoil pressure leading to the decrease of re-deposited material remaining on the hole sidewall. The following equation can be used to predict the maximum plasma ablation pressure P in the liquid confined region [30]:

$$P(\text{GPa}) = 0.01\sqrt{\frac{\alpha}{2\alpha + 3}} \times \sqrt{Z}(\text{g}/(\text{cm}^2\text{s})) \times \sqrt{I_0}(\text{GW}/\text{cm}^2)$$

(17)

where α is the scaling factor of intrinsic energy devoted to heat energy (typically $\alpha = 0.1 \sim 0.2$). I_0 is the laser power density, and Z is the equivalent acoustic impedance between the target and the confining liquid which can be calculated using the following equations [31]:

$$\frac{2}{Z} = \frac{1}{Z_{\text{liquid}}} + \frac{1}{Z_{\text{target}}}$$

(18)

where Z_{liquid} and Z_{target} are the shock acoustic impedance of the chemical liquid and the Inconel 718 target respectively. $Z = \rho v$, ρ and v are the medium density and sound speed in the same medium. The density of the chemical liquid is 1.06 g/cm^3, and the acoustic velocity in the chemical liquid is 1.497×10^5 (cm/s). The density of Inconel 718 is 8.24 g/cm^3, and the acoustic velocity in Inconel 718 is 5.617×10^5 (cm/s). Hence, $Z_{\text{liquid}} = 0.159 \times 10^6$ (g/(cm^2 ·s)) for the chemical liquid and $Z_{\text{target}} = 4.63 \times 10^6$ (g/(cm^{2}s)) for the Inconel 718 target, $Z = 0.33 \times 10^6$ (g/(cm^{2}s)). When the laser power density is 6×10^9 (W/cm^2), the maximum plasma ablation pressure is estimated about $2.5 \sim 3.4$ GPa calculated from Eq. (17). The laser plasma ablation pressure provides a driving force for molten debris to expel out of the hole. As soon as the laser is switched off, the laser plasma begins to cool adiabatically. After a few microseconds, the laser plasma pressure begins to weaken and finally annihilates.

4.2 The Flow Field Evolution in the Liquid Confined Region at the Second Stage

The pressure field color map (Unit: Pa) and velocity color map (Unit: m/s) at different moments are presented in Figs. 6, 7, which supply the information including the change of bubble shape, the evolution of pressure distribution, fluid flow direction, and velocity. The velocity vectors give the direction of the flow field. The black solid line represents the gas–liquid interface. The plasma distinguishes in the cavity and forms an initial bubble. A small initial bubble appears on the target surface within 1 μs. In Fig. 6a, the high temperature and high-pressure gas/plasma expand outward. The cavitation bubble expands to its maximum diameter at
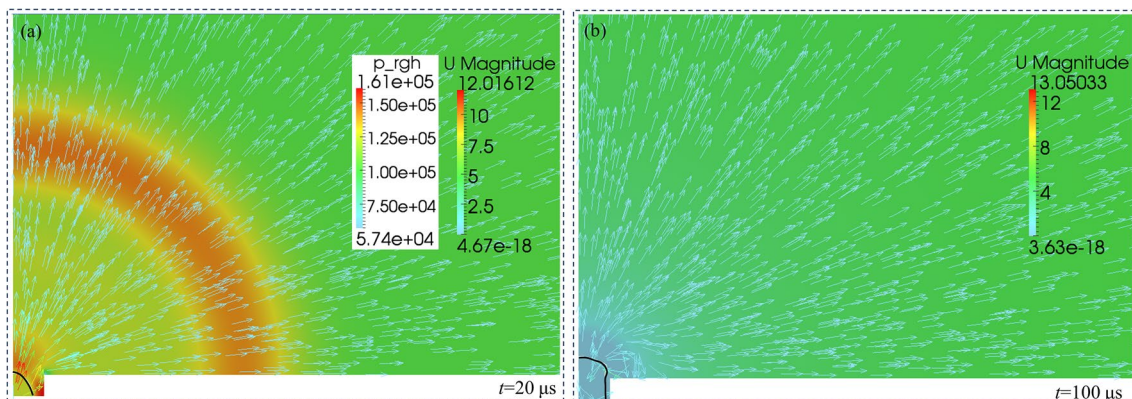

Fig. 6 The pressure field color map (Unit: Pa) and velocity color map (Unit: m/s) at different moments during the expansion of the cavitation bubble
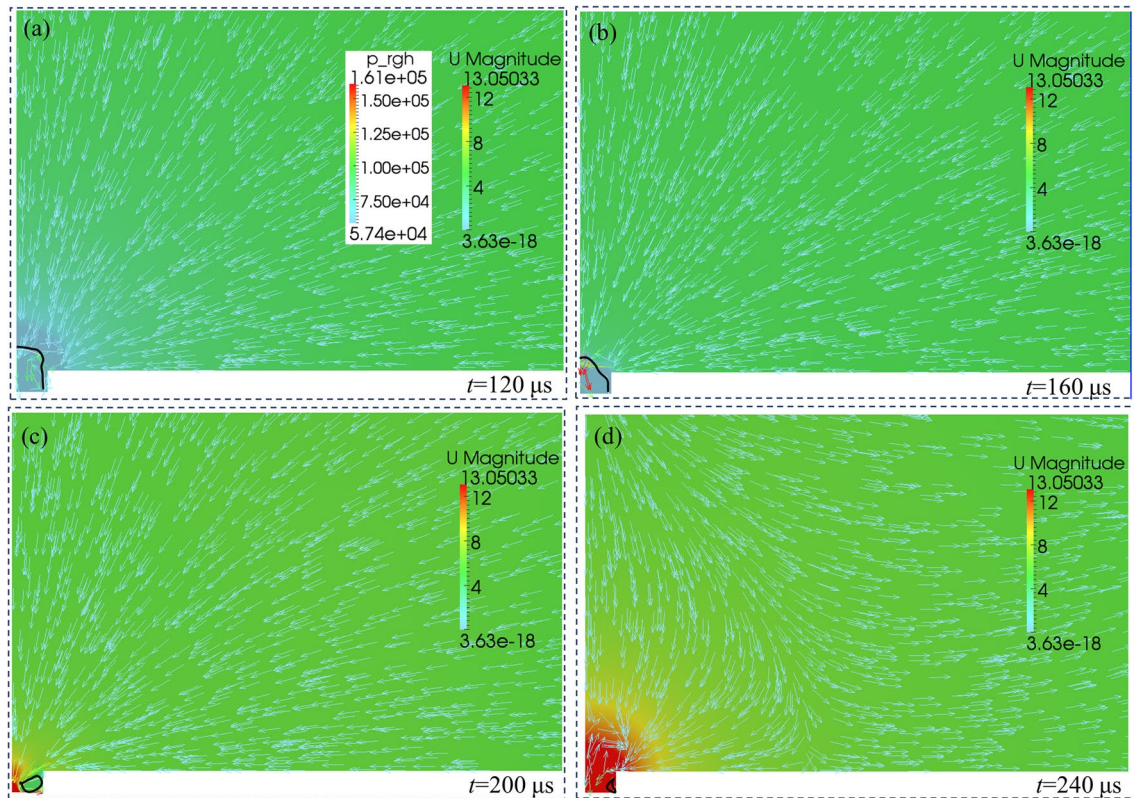
Fig. 7 The pressure field color map (Unit: Pa) and velocity color map (Unit: m/s) at different moments during the shrinkage of the cavitation bubble

100 µs, as presented in Fig. 6b. Then it begins to shrink because of the pressure difference between the bubble and the ambient pressure and the inertial effects after 100 µs, as presented in Fig. 7a. The cavitation bubble continues to shrink at 160 µs in Fig. 7b. When the pressure inside the bubble drops to a sub-atmospheric level, the bubble starts to collapse leading to a high-speed liquid jet followed by a secondary shock wave at 200 µs, as shown in Fig. 7c. The cavitation bubble expansion and collapse cycle with a maximum bubble radius last for 200 µs. The numerical simulation result shows that the maximum radius bubble appears at 100 µs. In our previous study [23], the maximum radius bubble is detected experimentally on the target surface at 104 µs in water. The experiment results in Ref. [32, 33] found the bubble reaches its maximum radius at 100~207 µs for liquid depths of 5 mm. Comparing the numerical results with these experimental results, the numerical simulation results in this study are reasonable. In Fig. 7, it can be seen that after the collapse of the cavitation bubble, the liquid jet pierces through the bubble and hits the hole's inner wall and bottom with a maximal impact pressure of ~ 161 kPa and a micro-liquid jet velocity of ~ 13 m/s at 200 µs. Driven by the liquid jet, the chemical liquid jet impinges onto the hole's inner wall and bottom and etches off a part of the softening

layer material. The liquid jet impact pressure does not provide enough upward eruption velocity for the large molten particles from the hole, and chemical etching morphology is determined by the jet shape and trail. Thus, the depth of the hole and the hole taper increase.

4.3 Analysis of Interaction Mechanism in High-temperature Chemical Assisted Laser Processing

In the process of high-temperature chemical assisted laser processing, laser-induced plasma occurs in the initial few hundred nanoseconds. The plasma ablation pressure is on the order of GPa and lasts a few microseconds until the plasma gradually attenuates and annihilates. The plasma ablation pressure effectively enhances the material removal along the hole depth with considerably less material residue redeposition on the hole wall, which reduces the hole taper. The bubble pulsation period, which includes the process of expansion, shrinkage, collapse, and rebound, is a few hundred microseconds. A liquid jet emerging from the cavitation bubble collapse occurs after 0.1 ms. The effect of cavitation action on the solid boundary nearby results from the shock waves and liquid jets produces when the bubbles collapse.

The liquid jet provides a driving force for chemical liquid inject into the micro-hole again. This stage lasts about a few hundred microseconds until the cavitation bubble rebound disappears.

Therefore, as shown in Fig. 8, when the laser pulse interval is 0.1 ms, the pulse interval is too short, the liquid jet effect has not yet been completely shown, and the next adjacent pulse work again to provide plasma ablation pressure. Under an impact force of the order of GPa magnitude, the molten particles are expelled from the hole and react with the chemical liquid to generate a gas and byproducts that can be dissolved in water, minimizing the possibility of re-deposition on the surface. Meanwhile, the chemical etching in the local high-temperature environment promotes the sidewall material removal. Therefore, the hole has a cylindrical shape with minimal surface roughness. When the pulse interval is 1 ms, the pulse interval is long enough that the liquid jet effect is completely displayed. The jet pushes the chemical liquid into the hole and etches off the softening layer material on the sidewall. The chemical etching morphology is determined by the jet shape. The liquid jet impact pressure (kPa ~ MPa) does not provide enough upward eruption velocity for the large deposition particles from the hole. Therefore, the hole depth increases, and the taper angle also increases affected by the chemical liquid jet.

5 Conclusions

The high-temperature chemical assisted laser processing was proposed to supply an one-step in-situ method for processing micro holes with characteristics of less thermal damage, lower taper, and no recast layer. To analyze the interaction mechanism, the pressure generated by laser plasma in the liquid confined region was estimated theoretically, and the evolution of the flow dynamic was calculated numerically. The main results of this study are as follows:

(1) The focus position in the chemical liquid shifted downward as the result of light refraction and vapor-plasma plume. When the liquid layer thickness was 5 mm, the focus position was shifted down by approximately 1 mm.

(2) The interval between two adjacent pulses had a great impact on the hole shape. When the laser pulse interval was 0.1 ms, the blind hole shape was close to being cylindrical with a taper angle of 13°. When the laser pulse interval was 1 ms, the blind hole was a conical shape with a taper angle of 50°.

(3) In laser direct processing in the air, the ejected material re-deposited at the hole entrance, and the surface roughness of hole entrance S_a was about 8.76 μm. In

Fig. 8 Schematic diagram of the interaction mechanism and hole evolution process. **a** The laser pulse interval is 0.1 ms. **b** The laser pulse interval is 1 ms
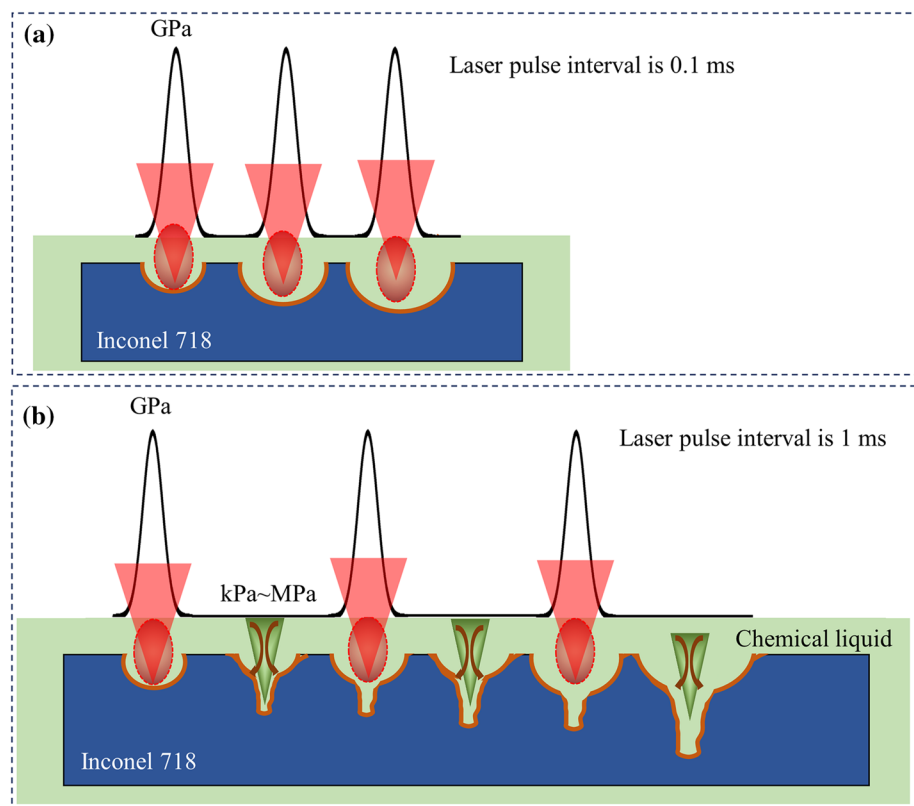
high-temperature chemical assisted laser processing, there was no obvious residual debris and recast layer deposited on the hole entrance, the surface roughness of the hole entrance S_a was about 0.42 μm. Therefore, high-temperature chemical assisted laser processing can effectively improve the hole surface quality by reducing the recast layer formation and surface roughness.

(4) The micro-hole morphology was related to the duration time of the laser plasma ablation pressure in the liquid confined region and the starting time of the liquid jet. The plasma ablation pressure was on the order of GPa and lasted a few microseconds, which enhanced the material removal along the hole depth and reduced the hole taper. The liquid jet emerging from the cavitation bubble collapse occurred after 0.1 ms which influenced the chemical etching shape.

In conclusion, the high-temperature chemical assisted laser processing supplies a more gentle method for noticeably optimizing hole shape, improving drilling quality, and reducing the recast layer formation, compared with laser direct processing. This technology could be a potential method for machining nickel alloy or other thermal-sensitive materials.

Declarations

Conflicts of interest The authors declare that there is no conflict of interest.

References

1. F.Y. Zhang, J. Wang, X. Wang, J. Zhang, Y. Hayasaki, D. Kim, S.F. Sun, Opt. Laser Technol. **143**, 107335 (2021). https://doi.org/10.1016/j.optlastec.2021.107335
2. Z.N. Yang, P.F. Ji, Z. Zhang, Y.D. Ju, Z. Wang, Q. Zhang, C.C. Wang, W. Xu, Opt. Commun. **475**, 126237 (2020). https://doi.org/10.1016/j.optcom.2020.126237
3. J.M. Silva, F. Ferreira, S.M. Abreu, J.E. Matos, L.M.P. Durãoa, Compos. Struct. **181**, 306–314 (2017). https://doi.org/10.1016/j.compstruct.2017.08.080
4. F.H. Caki, O.N. Celik, Met. Mater. Int. **27**, 3529–3537 (2021). https://doi.org/10.1007/s12540-020-00667-z
5. T.J. Chen, B.Q. Yang, Met. Mater. Int. **27**, 5299–5313 (2021). https://doi.org/10.1007/s12540-020-00775-w
6. X.S. Jia, J. Dong, Y.Q. Chen, H.L. Wang, G.Z. Zhu, K. Aleksei, X. Zhu, Opt. Lett. **45**, 1691–1694 (2020). https://doi.org/10.1364/OL.383207
7. W. Perrie, A. Rushton, M. Gill, P. Fox, W. O'Neill, Appl. Surf. Sci. **248**, 213–217 (2005). https://doi.org/10.1016/j.apsusc.2005.03.005
8. N. Ren, K.B. Xia, H.Y. Yang, F.Q. Gao, S.W. Song, Ceram. Int. **47**, 11465–11473 (2021). https://doi.org/10.1016/j.ceramint.2020.12.274
9. L.M. Wee, E.Y.K. Ng, A.H. Prathama, H. Zheng, Opt. Laser Technol. **43**, 62–71 (2011). https://doi.org/10.1016/j.optlastec.2010.05.005
10. V. Tangwarodomnukun, P. Likhitangsuwat, O. Tevinpibanphan, C. Dumkum, Int. J. Mach. Tool. Manu. **89**, 14–28 (2015). https://doi.org/10.1016/j.ijmachtools.2014.10.013
11. S. Mullick, Y.K. Madhukar, S. Roy, A.K. Nath, Int. J. Mach. Tool. Manu. **91**, 62–75 (2015). https://doi.org/10.1016/j.ijmachtools.2015.02.005
12. V. Tangwarodomnukun, J. Wang, C.Z. Huang, H.T. Zhu, Int. J. Mach. Tool Manu. **79**, 1–16 (2014). https://doi.org/10.1016/j.ijmachtools.2013.12.003
13. C. Deng, H. Yeo, H. Ki, Opt. Express **28**, 11128–11143 (2020). https://doi.org/10.1364/OE.389497
14. Y. Liu, M.R. Wei, T. Zhang, H.C. Qiao, H. Li, Opt. Laser Technol. **137**, 106820 (2021). https://doi.org/10.1016/j.optlastec.2020.106820
15. V. Khuat, Y.C. Ma, J.H. Si, T. Chen, F. Chen, X. Hou, Appl. Surf. Sci. **289**, 529–532 (2014). https://doi.org/10.1016/j.apsusc.2013.11.030
16. B. Lia, W.F. Sun, X. Xiang, X.L. Jiang, W. Liao, H.J. Wang, X.D. Yuan, X.D. Jiang, X.T. Zu, J. Mater. Sci. Technol. **19**, 3231–3240 (2022). https://doi.org/10.1016/j.jmrt.2022.06.061
17. T. Chen, A. Pan, C.X. Li, J. Si, X. Hou, Appl. Surf. Sci. **325**, 145–150 (2015). https://doi.org/10.1016/j.apsusc.2014.11.012
18. H. Zhu, Z.Y. Zhang, K. Xu, J.L. Xu, S.J. Zhu, A.B. Wang, H. Qi, Materials **12**, 41 (2018). https://doi.org/10.3390/ma12010041
19. A. Vogel, J. Noack, G. Hüttman, G. Paltauf, Appl. Phys. B **81**, 1015–1047 (2005). https://doi.org/10.1007/s00340-005-2036-6
20. C.L. Zheng, H. Shen, J. Manuf. Process. **73**, 354 (2022). https://doi.org/10.1016/j.jmapro.2021.11.020
21. Q. Zhang, S.F. Sun, F.Y. Zhang, J. Wang, Q.Q. Lv, Y. Shao, Q.Y. Liu, J. Shao, X.F. Liu, Y. Zhang, Int. J. Adv. Manuf. Tech. **106**, 155–162 (2020). https://doi.org/10.1007/s00170-019-04541-0
22. B. Han, K. Köhler, K. Jungnickel, R. Mettin, W. Lauterborn, A. Vogel, J. Fluid Mech. **771**, 706–742 (2015). https://doi.org/10.1017/jfm.2015.183
23. B. Han, R.H. Zhu, Z.Y. Guo, L. Liu, X.W. Ni, Eur. J. Mech. B-Fluid **72**, 114–122 (2018). https://doi.org/10.1016/j.euromechflu.2018.05.003
24. S.C. Feng, C.Z. Huang, J. Wang, H.T. Zhu, Mat. Sci. Semicon. Proc. **82**, 112–125 (2018). https://doi.org/10.1016/j.mssp.2018.03.035
25. P. Wang, Z. Zhang, D.H. Liu, W.Z. Qiu, Y. Zhang, G.J. Zhang, Opt. Laser Technol. **151**, 108022 (2022). https://doi.org/10.1016/j.optlastec.2022.108022
26. Q. Tang, C.J. Wu, T.H. Wu, Opt. Commun. **478**, 126410 (2021). https://doi.org/10.1016/j.optcom.2020.126410
27. J. Lv, X. Dong, K.D. Wang, W.Q. Duan, Z.J. Fan, X.S. Mei, Int. J. Adv. Manuf. Tech. **86**, 1443–1451 (2016). https://doi.org/10.1007/s00170-015-8279-4
28. S.S. Mao, X.L. Mao, R. Greif, R.E. Russo, Appl. Phys. Lett. **77**, 2464 (2000). https://doi.org/10.1063/1.1318239

29. Z. Zhang, Z. Xu, C.C. Wang, S.Y. Liu, Z.N. Yang, Q. Zhang, W. Xu, Opt. Laser Technol. **139**, 106968 (2021). https://doi.org/10.1016/j.optlastec.2021.106968

30. M. Dell'Aglio, A.D. Giacomo, Appl. Surf. Sci. **515**, 146031 (2020). https://doi.org/10.1016/j.apsusc.2020.146031

31. R. Fabbro, J. Fournier, P. Ballard, D. Devaux, J. Virmont, J. Appl. Phys. **68**, 775–784 (1990). https://doi.org/10.1063/1.346783

32. T.T.P. Nguyen, R.T. Yamagishi, Y. Ito, Opt. Lasers Eng. **126**, 105937 (2020). https://doi.org/10.1016/j.optlaseng.2019.105937

33. J.Y. Long, M.H. Eliceiri, Y.X. Ouyang, Y.K. Zhang, X.Z. Xie, C.P. Grigoropoulos, Opt. Lasers Eng. **137**, 106334 (2021). https://doi.org/10.1016/j.optlaseng.2020.106334